

# AGN フィードバック効率のウィンドマッハ数依存性 Dependence of the AGN Feedback Efficiency on the Wind Mach Number

理工学群 物理学類 (201613021) Xue YunFan

指導教官 : Alexander Wagner

## 概要

We perform two-dimensional spherically-polar hydrodynamic simulations of AGN winds interacting with the interstellar medium of galaxies on scales ranging from 10 pc to 3 kpc, and explore the dependence of the efficiency of AGN feedback on the internal Mach of the wind for winds of identical power. The Mach number is a measure of the ratio of kinetic energy to enthalpy in the wind. Five different measures of the AGN feedback efficiency with regard to the dispersed interstellar clouds are employed: 1) the remaining mass, 2) the velocity reached, 3) the mass outflow rate, 4) the kinetic energy, and 5) the momentum boost. We find that higher Mach number winds lead to a stronger destruction of clouds, but the runs show variations of only up to approximately 50% in velocity and mass outflow rate, while the kinetic energy of accelerated clouds reaches 10% of the injected jet energy in almost all simulations. Low Mach-number enthalpy-dominated winds can provide clouds with a large momentum boost via pressure gradients, which is less destructive to the clouds. While exhibiting interesting trends, the variation in efficiency due to differences in internal Mach number are likely secondary compared to those due to the properties of the interstellar medium. The simulations presented in this work, although conducted at low-resolution, motivate high-resolution three-dimensional simulations on comparable spatial scales.

# 1 Introduction

In the center of every galaxy, there may exist a supermassive black hole (SMBH) emitting strong radiation or streams of high-velocity plasma in the form of a wind or a jet. A galaxy, and in particular its nuclear region, with such an “active” central SMBH is termed an active galactic nucleus (AGN). The bolometric luminosity of an AGN, which includes the total radiative luminosity and the kinetic luminosity of the wind or jet, is often comparable or greater than the stellar luminosity of the galaxy. Typically, galactic nuclei with luminosities exceeding  $10^{42} \text{ erg s}^{-1}$  are considered to be AGN.

The energy released by the AGN comes from the gravitational energy of matter accreting through the galaxy toward the central black hole. Sometimes, a powerful jet is launched from the environs of the black hole that can propagate at nearly the speed of light through the galaxy and into the halo of the galaxy, interacting with the interstellar and intergalactic medium. Other times, the accretion flow forms a highly magnetized accretion disc around the SMBH. The strong radiation and magnetic fields in the accretion disc can launch powerful winds that expand into and interact with the interstellar medium (ISM) of the galaxy. The effect of such winds are the focus of this study.

An AGN wind carrying energy and momentum strongly affects the host galaxy by transferring some of this energy and momentum to the ISM. In particular, the dense, cold phase of the ISM consisting of atomic and molecular clouds are strongly affected. The wind can shock, compress, and disperse clouds, leading to a change in cloud properties and star forming across the entire galaxy. These effects are collectively called active galactic nucleus feedback.

AGN feedback plays a very important role in galaxy formation (Naab & Ostriker, 2017), in particular at high redshifts ( $z \sim 2$ ), the peak of galaxy formation and black hole growth (Harrison et al., 2018). It is believed that AGN feedback is the principal mechanism for creating a causal link between the evolution of the central SMBH and the evolution of the galaxy as a whole on kpc scales (Silk & Rees, 1998; Fabian, 1999; King, 2003). Observationally, SMBH and galaxies appear to be locked in co-evolution (Rodighiero et al., 2015; Schindler et al., 2016). One of the most important manifestations of SMBH galaxy co-evolution is the  $M$ - $\sigma$  relation, the tight correlation between SMBH mass and velocity dispersion of the bulge in a galaxy (Ferrarese & Merritt, 2000; McConnell & Ma, 2013).

Current day cosmological simulations (Weinberger et al., 2018) are capable of simulating the evolution of galaxies in a representative cosmological volume, although these simulations must

rely on sub-grid models for star-formation, black hole growth, and their respective feedback processes, supernova feedback and AGN feedback, because the galaxies are only marginally resolved. The detailed interactions between outflows and the ISM are not fully captured, leading to errors in the energy balance in the ISM gas and over- or under-efficient AGN feedback. As a result, the rate of energy injection into the ISM by AGN are fine-tuned to reproduce the present-day  $M$ - $\sigma$  relation and galaxy luminosity functions.

Simulations of AGN feedback in isolated galaxies with idealized initial conditions attempt to improve this situation: [Wagner & Bicknell \(2011\)](#), [Wagner et al. \(2012, 2013, 2016\)](#), [Bieri et al. \(2017\)](#) and [Mukherjee et al. \(2016, 2018\)](#) performed three-dimensional simulations of AGN jets and winds interacting with a gas-rich, multi-phase, ISM. The studies investigated the relationship between feedback efficiency and various parameters pertaining to the ISM and the AGN, including the AGN power, the density, spatial distribution, and clumpiness of the ISM. An important ingredient in these simulations was the realistic modelling of a multiphase, inhomogeneous ISM, on whose properties the feedback efficiency strongly depended. However, the relationship between an AGN wind's Mach number and the feedback efficiency has not been tested.

This study will examine the dependence of the AGN feedback efficiency as determined by five differing measures on the internal Mach number of the wind through a series of 2 dimensional spherically polar axisymmetric hydrodynamic simulations. As will be described in the next section, the internal Mach number of the wind is a measure of the fraction of kinetic energy and the fraction of enthalpy in a wind, which is expected to lead to different dissipation histories in the outflow, which in turn may lead to different rates of transfer of energy from the wind to the ISM. The Mach number is also of interest because of the different turbulent properties that subsonic and supersonic flows exhibit ([Smits et al., 1989](#)). The next section will also explain how the simulations are set up and how the Mach number relates to other thermodynamic quantities of the wind. Section 3 presents the results of the simulations, and Section 4 provides a summary and discussion of the results.

## 2 Methods

In this study, we focus on the interaction of a powerful AGN wind with a massive, gas-rich, forming galaxy, typically encountered at redshifts  $z = 2$  to  $z = 3$ . The setup of the simulations is highly idealized.

1. We only focus on the gas dynamics of the galaxy using hydrodynamical simulations.

2. The galaxy is morphologically quasi-spherical.
3. A spherical wind is injected at the center of the galaxy, where a SMBH is thought to reside.

The methods employed in this work are similar to those in [Wagner et al. \(2013\)](#), with some simplifications, most notably that the hydrodynamic simulations are conducted in 2D spherical-polar coordinates at low resolutions.

AGN disc winds have never been directly observed, but are inferred from absorption of the AGN radiation by fast outflows. Although the mechanisms of how AGN disc winds are accelerated are not well known, and although the structure of the interstellar medium in galaxies, particularly at high-redshifts, is also not well constrained, a simplified and idealized galaxy model can help to understand the effects of AGN winds on the interstellar medium.

The wind – ISM interactions in our model galaxies are modeled using hydrodynamic simulations. The interaction of the AGN wind and the gas in the galaxy involves three gas components, which are treated as a single fluid: 1) The AGN wind plasma, 2) the hot, diffuse gas of the galactic halo, and 3) the dense warm clouds embedded in the hot halo.

The governing equations and computational code are described first, followed by the setup and components of the model galaxy.

## 2.1 Hydrodynamical code PLUTO

PLUTO is a freely-distributed software for the numerical solution of mixed systems targeting high Mach number flows in astrophysical fluid dynamics. PLUTO solves the fundamental hydrodynamical equations for our problem:

$$\begin{aligned}
\frac{\partial \rho}{\partial t} + \nabla \cdot (\rho \mathbf{v}) &= 0, \\
\frac{\partial \rho \mathbf{v}}{\partial t} + \nabla \cdot (\rho \mathbf{v} \mathbf{v} + p \mathbf{I}) &= 0, \\
\frac{\partial}{\partial t} \left( \frac{1}{2} \rho \mathbf{v} \cdot \mathbf{v} + \frac{1}{\gamma - 1} p \right) + \nabla \cdot \left[ \mathbf{v} \left( \frac{1}{2} \rho \mathbf{v} \cdot \mathbf{v} \frac{\gamma}{\gamma - 1} p \right) \right] &= -\rho^2 \Lambda(T), \\
p &= \rho k T / \mu.
\end{aligned}$$

$\rho, \mathbf{v}, p, I, T, \Lambda, \phi, \gamma = 5/3, k, \mu$  are the fluid density, the velocity vector, the pressure, the unit tensor, the temperature, the cooling rate, the gravitational potential, the adiabatic index for an ideal gas, Boltzmann's constant and the mean mass per particle, respectively. In the code we

solve two further mass conservation equations: one for the advected tracer tracing the wind, and one for the advected tracer tracing clouds. The tracer variable for the cloud is commonly used in the analysis of the simulations to trace the evolution of the clouds that existed at  $t = 0$ . A cloud tracer cut of 0.98 is applied in the analysis when identifying clouds at  $t > 0$ . Only cells that retain sufficient original cloud material are considered as remaining clouds.

For simplicity, gravity is not included in the simulations in this work, but radiative cooling is. The radiative cooling function is obtained from a MAPPINGS V (Sutherland & Dopita, 2017) non-equilibrium ionization simulation that includes recombination line cooling of hydrogen, helium, and metals (oxygen, carbon, sodium, silicon, iron etc) assuming solar abundances, as well as Bremsstrahlung. The temperature range for which cooling is invoked is from 300 K to  $10^{11}$  K. The cooling floor at 300 K is set for numerical reasons and does not affect the results. Initially cells can have temperatures less than 300 K however.

We use PLUTO version 4.3 to simulate AGN winds interacting with the interstellar medium of galaxies on scales ranging from 10 pc to 3000 pc on a two-dimensional spherically-polar grid. The PLUTO code is a Godunov-type code and we use the piece-wise parabolic method by Colella & Woodward (1984) and the HLLC Riemann solver to calculate fluxes. All source terms are operator-split. The temporal integration uses a third order Runge-Kutta scheme.

The simulations were run on an Ubuntu (version 19.04) Linux (5.0.0-21-generic) x86\_64 laptop (version 19.04) using 5 Intel i7-8750H cores with two threads each and 32 GB of DDR4 RAM. Each simulation required a walltime of approximately 15 minutes to complete.

## 2.2 Initial and boundary conditions

### 2.2.1 Components of the galaxy

In our 2D simulations, we chose spherically-polar coordinates and the grid and boundary conditions are as follows: the radial  $r$ -axis starts from 10 pc and goes to 3000 pc; the polar  $\theta$ -axis starts from  $0^\circ$  to and goes to  $180^\circ$ . The wind is injected at the base of the  $r$ -axis uniformly at all angles  $\theta$  – it is a spherical wind with outflow boundary conditions at  $r = 10$  kpc. The conditions around the black hole are not considered, and at the base the wind always has constant values of density, velocity, and pressure. In the polar direction,  $\theta$  extends to  $180^\circ$  to cover both hemispheres in order to avoid numerical effects near the equatorial plane of symmetry. For the outer boundary in  $r$  we impose outflowing boundary conditions.

For the boundary at  $\theta = 0$  and  $\theta = 180^\circ$  we impose axis-symmetric boundary conditions.

The parameters pertaining to the interstellar medium we set in this series of simulations are

the same for all simulations. The interstellar medium consists of a diffuse hot phase, the hot halo that fills the entire computational volume, and a clumpy warm dense phase, that extends initially to a radius of 0.6 kpc.

### 2.2.2 Interstellar medium parameters

The hot halo parameters are as follows: The ambient density and temperature are initially uniform in the entire computational volume with values  $n_a = \rho_a/(\mu u) = 1 \text{ cm}^{-3}$  and  $T_a = 10^7 \text{ K}$ , respectively. The quantity  $\mu u$  is the mean mass per particle, and we choose  $\mu = 0.60364$ , typical for a fully ionized interstellar medium (Sutherland & Dopita, 2017).

The warm clouds are initialized as in Sutherland & Bicknell (2007). A fractal density field with log-normal single point statistics is generated through Fourier transform of a Gaussian random field according to the method by Lewis & Austin (2002). The fractal density field that forms the clouds is multiplied by a mean density for the clouds of  $300 \text{ cm}^{-3}$ . Setting the clouds in pressure equilibrium with the hot halo yields a temperature for each cloud cell. If the temperature of the cell exceeds  $3 \times 10^4 \text{ K}$ , the cloud gas is deemed thermally unstable and the cloud cell is replaced with the parameters of the hot halo. This creates a porous interstellar medium: warm clouds embedded in the hot halo.

### 2.2.3 Wind parameters

Consider a volume containing a plasma of density  $\rho_w$  and thermal pressure  $p_w$  moving with bulk velocity  $v_w$ . The kinetic energy density of the plasma in this volume is  $\rho_w v_w^2/2$  and the enthalpy is  $\gamma p_w/(\gamma - 1)$ . Let the power and the mass outflow rates of the wind denote the amount of plasma energy and mass, respectively, passing through the surface  $A$  bounding the volume with a bulk velocity  $v_w$  normal to  $A$ .

The power of the wind,  $L_w$ , and the mass outflow rate of the wind,  $\dot{m}_w$ , at the inlet are then:

$$L_w = \left( \frac{1}{2} \rho_w v_w^2 + \frac{\gamma p_w}{\gamma - 1} \right) v_w A \quad (1)$$

$$\dot{m}_w = \rho_w v_w A. \quad (2)$$

Combining Equations (1) and (2), we can express the wind density,  $\rho_w$ , and wind pressure,  $p_w$ , in terms of the wind power, mass outflow rate, and wind velocity,  $v_w$ :

$$p_w = \left( \frac{2L_w}{v_w} - \dot{m}_w v_w \right) \frac{\gamma - 1}{2\gamma A} \quad (3)$$

$$\rho_w = \frac{\dot{m}_w}{v_w A}. \quad (4)$$

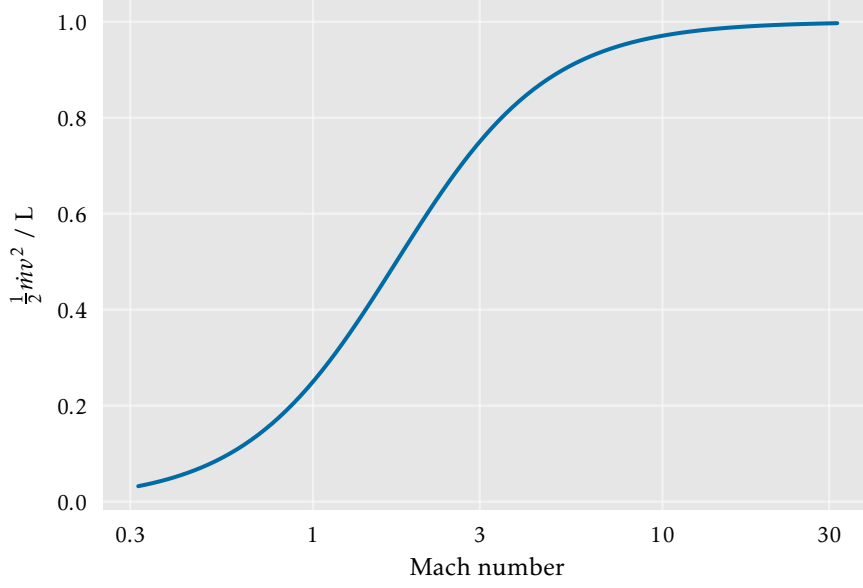


Fig. 1: Relationship between the wind Mach number and  $f_{\text{kin}}$ .

The internal Mach number of the wind is defined as:

$$M = \frac{v_w}{\sqrt{\gamma p_w / \rho_w}}. \quad (5)$$

Combining Equations (1), (2), and (6), we can also express the Mach number in terms of the wind power, mass outflow rate, and wind velocity.

$$M^2 = \left[ \frac{L_w}{\dot{m}_w v_w^2 / 2} - 1 \right]^{-1} \frac{2}{\gamma - 1}. \quad (6)$$

The ratio of kinetic energy to total power of the wind,  $f_{\text{kin}}$ , is

$$f_{\text{kin}} = \frac{\dot{m}_w v_w^2 / 2}{L_w} = \left[ 1 + \frac{2}{(\gamma - 1) M^2} \right]^{-1}. \quad (7)$$

The internal Mach number is, thus, a measure of the fraction of the wind energy that is in the form of kinetic energy. The relationship between the Mach number and  $f_{\text{kin}}$  is shown in Fig. 1.

In this work we shall vary the mass outflow rate of the wind as we vary the Mach number according to:

$$\dot{m}_w = \frac{L_w}{v_w^2 / 2} \left[ 1 + \frac{2}{(\gamma - 1) M^2} \right]^{-1}. \quad (8)$$

Looking at Fig. 2, there are many ways one could vary the Mach number. For example, one could move along an isobar (constant pressure) or isopycnal (constant density). One could also

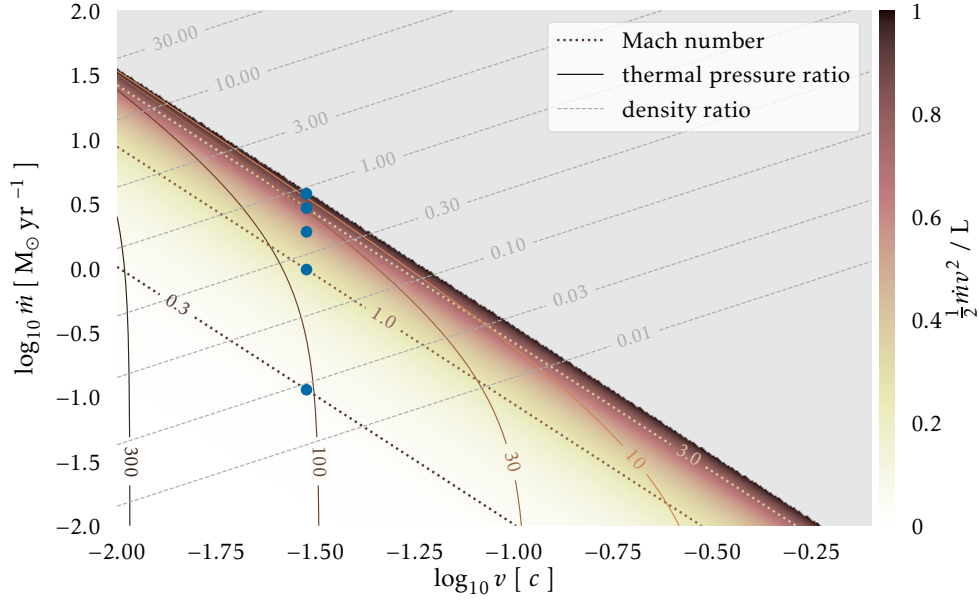


Figure 2: The parameter space of wind properties. The blue circles are the five simulations A to E (from bottom to top) presented in this work. See also Table 1 for the simulation parameters.

keep the velocity constant or keep the mass outflow rate of the wind constant. Finally one could also move along the gradient of the Mach number (or  $f_{\text{kin}}$ ) to minimize the change in wind parameters.

In this work, we keep the wind power and wind velocity constant at, respectively,  $L_w = 10^{44} \text{ erg s}^{-1}$  and  $v_w = 0.03c$ . While we vary the *internal* Mach number for different simulations, the constant wind velocity ensures that the *external* Mach number (the wind speed divided by the ambient sound speed) remains constant at approximately 20. Table 1 lists the simulation parameters for all the wind simulations performed.

As mentioned in §2.2.1, the ambient density and temperature are uniform with values  $n_a = 1 \text{ cm}^{-3}$  and  $T_a = 10^7 \text{ K}$ , respectively.



Sim. ID	$M$	$\dot{m}_w [\text{M}_\odot \text{yr}^{-1}]$	$p_w/p_a$	$\rho_w/\rho_a$	$f_{\text{kin}}$
A	0.3	0.11363	104.55716	0.02671	0.02913
B	1.0	0.97533	80.77041	0.22923	0.25000
C	1.7	1.91423	54.85257	0.44989	0.49066
D	3.0	2.92598	26.92347	0.68768	0.75000
Da <sup>1</sup>	3.0	— " —	— " —	— " —	— " —
Dn <sup>2</sup>	3.0	— " —	— " —	— " —	— " —
E	10.0	3.78768	3.13671	0.89020	0.97087

表 1: The parameters for the simulations. ( $M, \dot{m}_w$  is Mach number of the wind, mass outflow rate of the wind,  $p_w, \rho_w$  is the wind density and pressure,  $p_a, \rho_a$  is the ambient density and pressure,  $f_{\text{kin}}$  is the ratio of kinetic energy to total power of the wind) <sup>1</sup>Da simulation without cooling. <sup>2</sup>Dn simulation without clouds.

### 3 Results

The evolution of clouds for  $M = 3$  (simulation D) are shown in Figs. 3, 4, and 5. The clouds are initially static, starting in pressure equilibrium with the surrounding medium (Fig. 3a). As the wind expands through the region of clouds, the clouds are shocked and pushed outward by the wind. As the process continues, the clouds become increasingly dispersed and most of the initial cloud complexes are destroyed. This process implies that the wind causes negative feedback with respect to possible star-formation in the clouds. This effect is most obvious in cloud velocity maps in 5. Although the clouds are accelerated outward, they tend to disappear at large radii, occupying only a few cells in the end. However, this may be the result from the cloud tracer cut, by which any cells containing less than 98% of the initial cloud mass will be discarded. As the initial cloud complexes are dispersed, they mix with the ambient hot medium and their total mass decreases. Although not included in these plots, new cool, dense gas forms from surrounding hot gas, which is why there are more cloud-like regions in the density and temperature maps compared to the cloud velocity map (see the dark-colored cells in the temperature and density maps of Fig 5 which show dense cool clouds that include the original clouds and the newly formed clouds. In this work, we concentrate on the survival and destruction of original clouds. The evolution of the mass in clouds is shown in Fig. 11.

The simulation without cloud as in Fig. 7 (the same conditions with run D but without clouds) is a control simulation, showing the two-shock structure of a spherical wind. Similarly, the simulation without cooling is another control simulation, shown in Fig. 8 (also the same conditions with run D but without cooling). In comparison with the run D, the clouds in run Da are more fragmented and dispersed. This is expected since cooling, which stabilized clouds against disruption, was precluded, and this comparison emphasizes the importance of cooling in clouds for AGN feedback and stars formation in surviving clouds.

Fig. 9 and Fig. 10 are the snapshot of different simulations at the same time. Fig. 11, Fig. 12, Fig. 13, Fig. 14, Fig. 15 depict the evolution of mass-weighted average cloud speed, cloud mass outflow rates, kinetic energy efficiency in outflowing clouds, momentum boost, respectively. The mass-weighted averaged velocity is  $\bar{v} = \sum_i \rho_i V_i v_i / \sum_i \rho_i V_i$ , where the summation is over all cells, and the area  $V_i$  is the cylindrically revolved volume of the a cell.

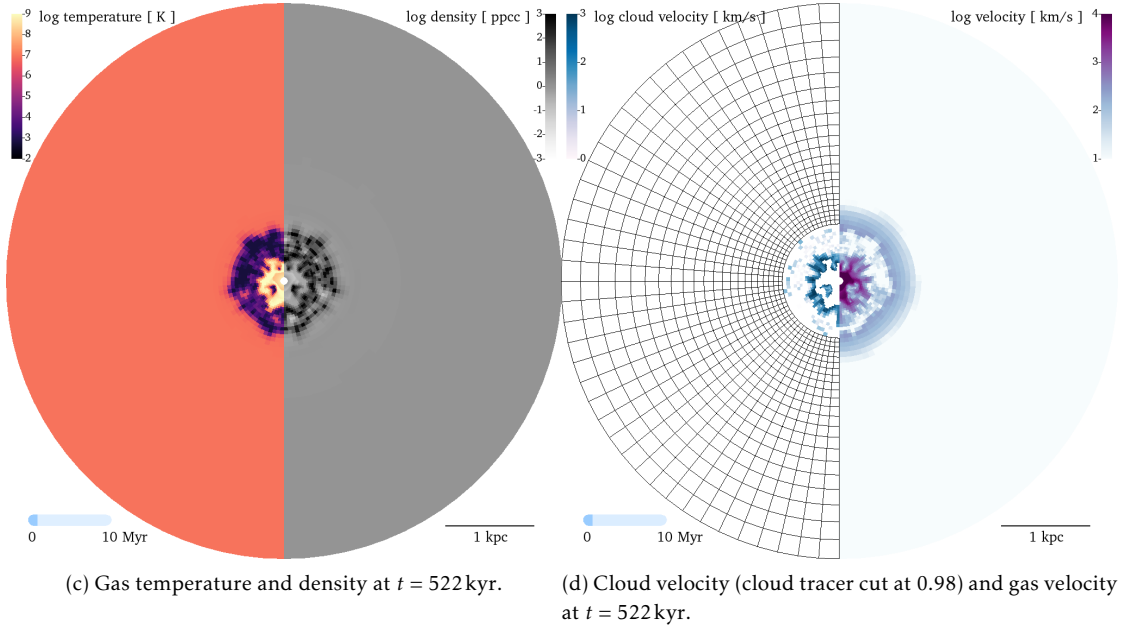
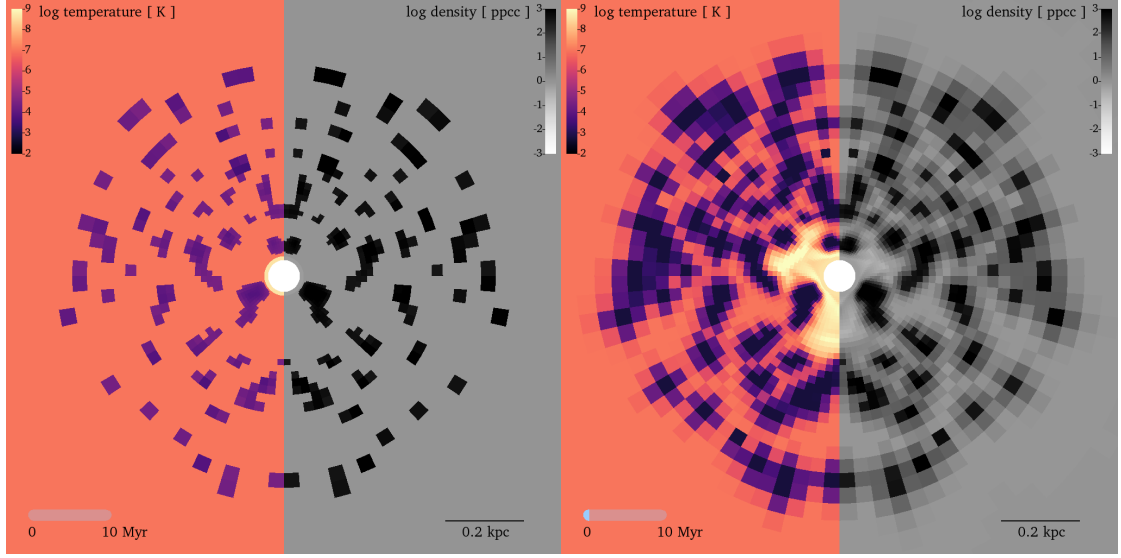


Figure 3: Initial conditions and early stages of simulation D, showing clouds were shocked by wind. The time zero snapshot(a) also reveal the initial conditions.

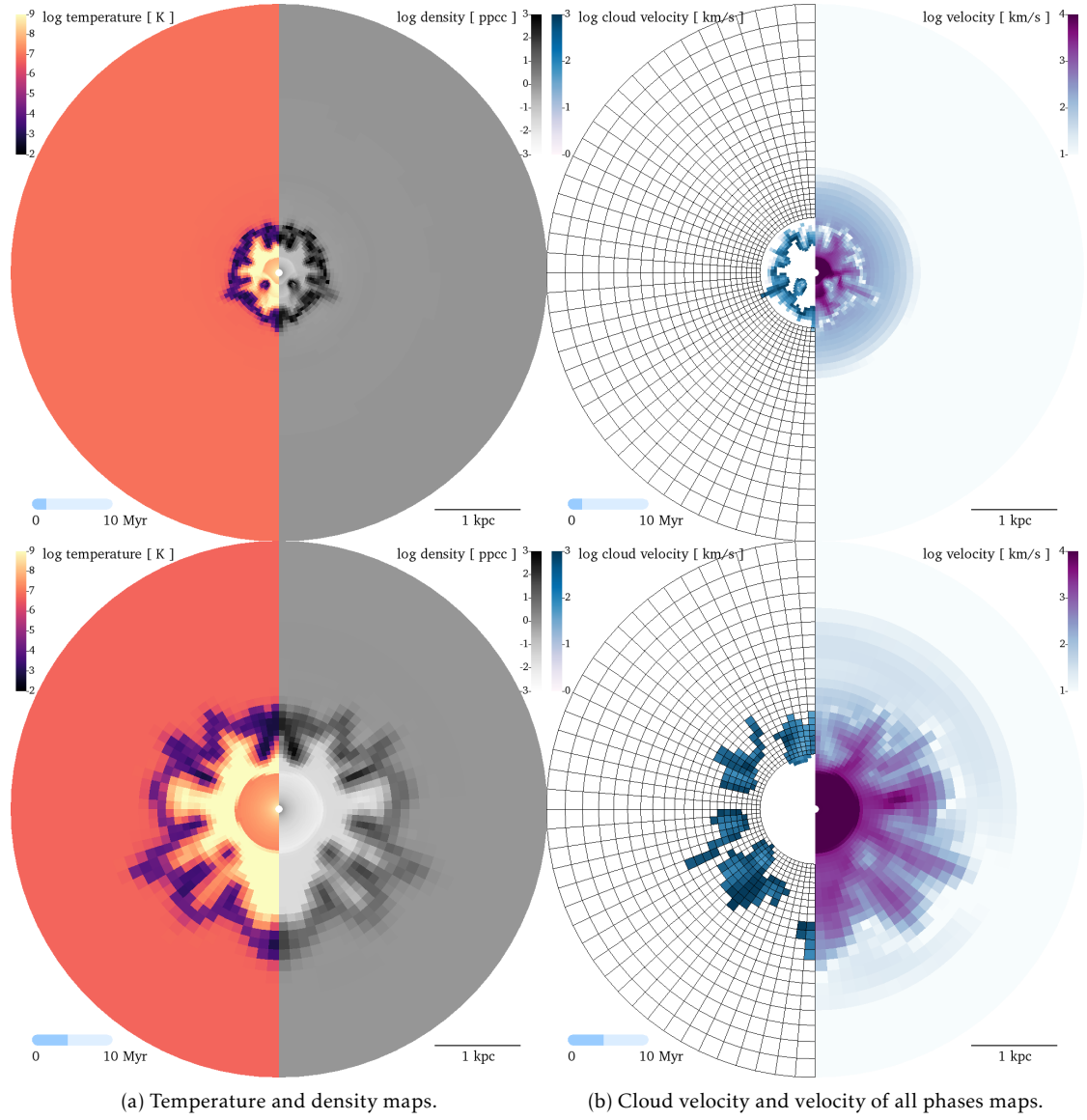


Figure 4: Intermediate stages of evolution of simulation D ( $t = 1240\text{kyr}$  top and  $4274\text{kyr}$  bottom), showing clouds were continuously pushed outward by wind.

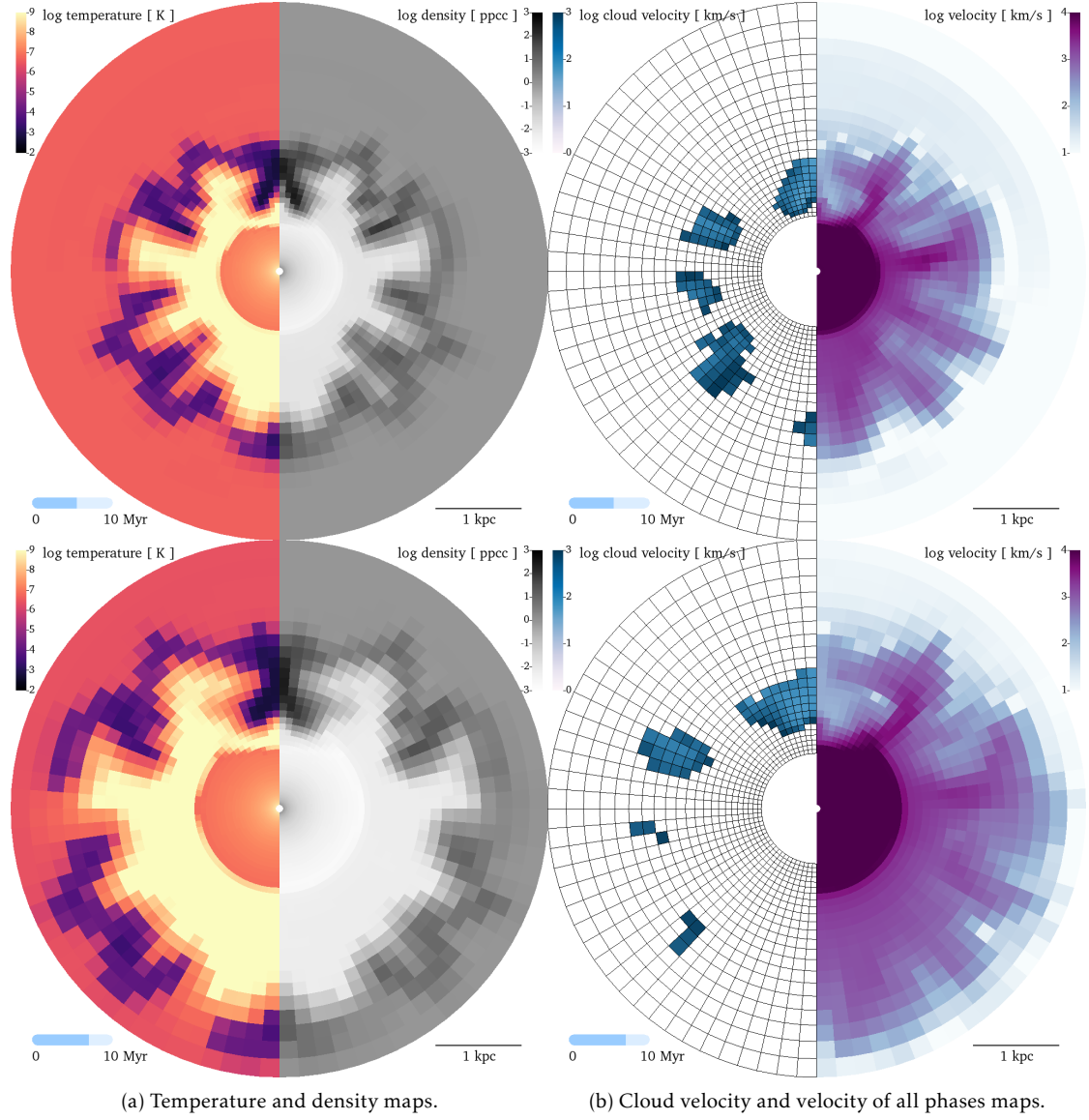


Figure 5: Advanced stages of evolution of simulation D ( $t = 5481$  kyr top and  $7210$  kyr bottom), showing how clouds were destroyed at late times.

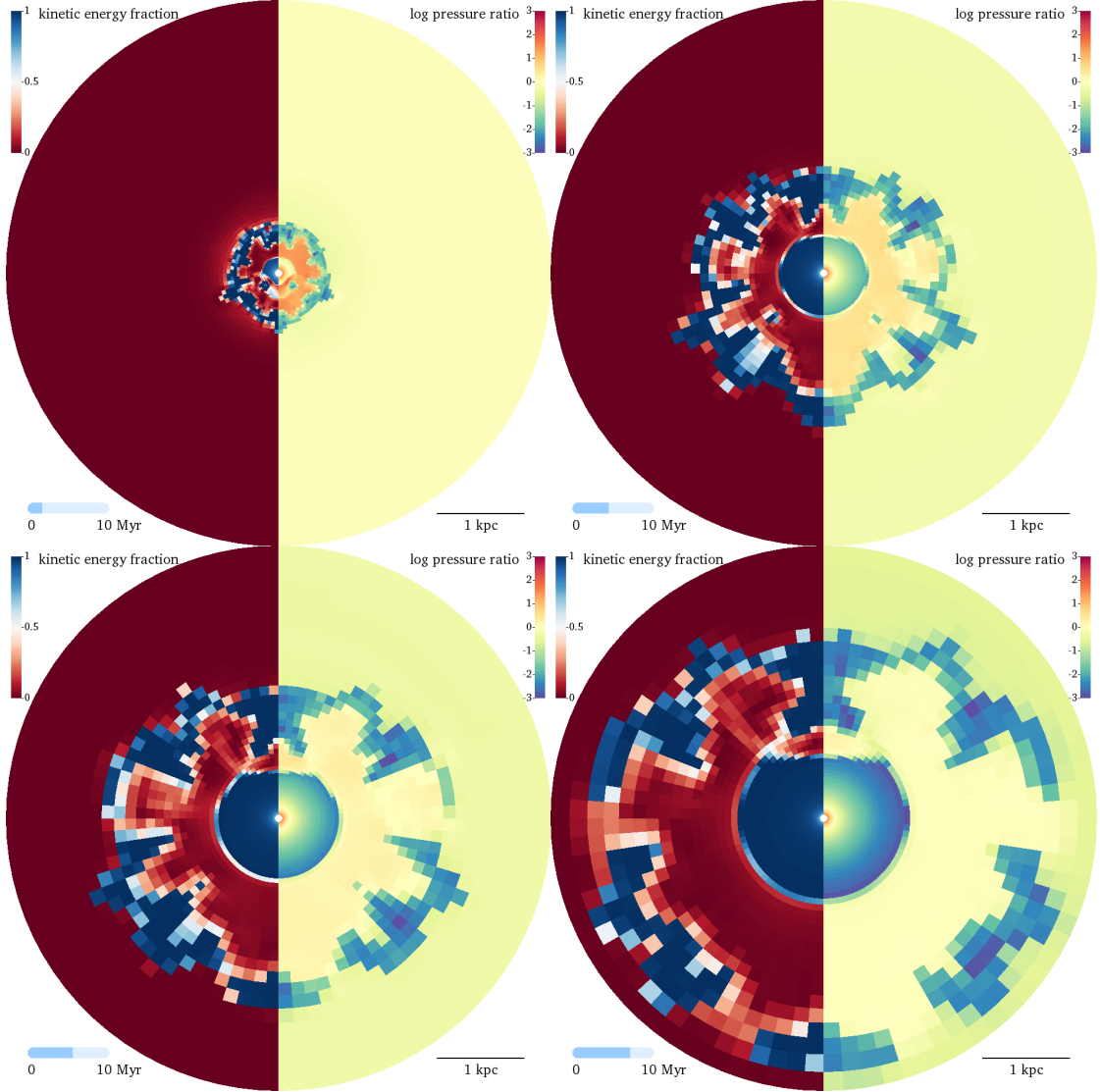


Figure 6: Maps of the evolution of the pressure and  $f_{\text{kin}}$  in Simulation D at  $t = 1240, 4275, 5482, 7212$  kyr (left top, right top, left bottom, right bottom, respectively).

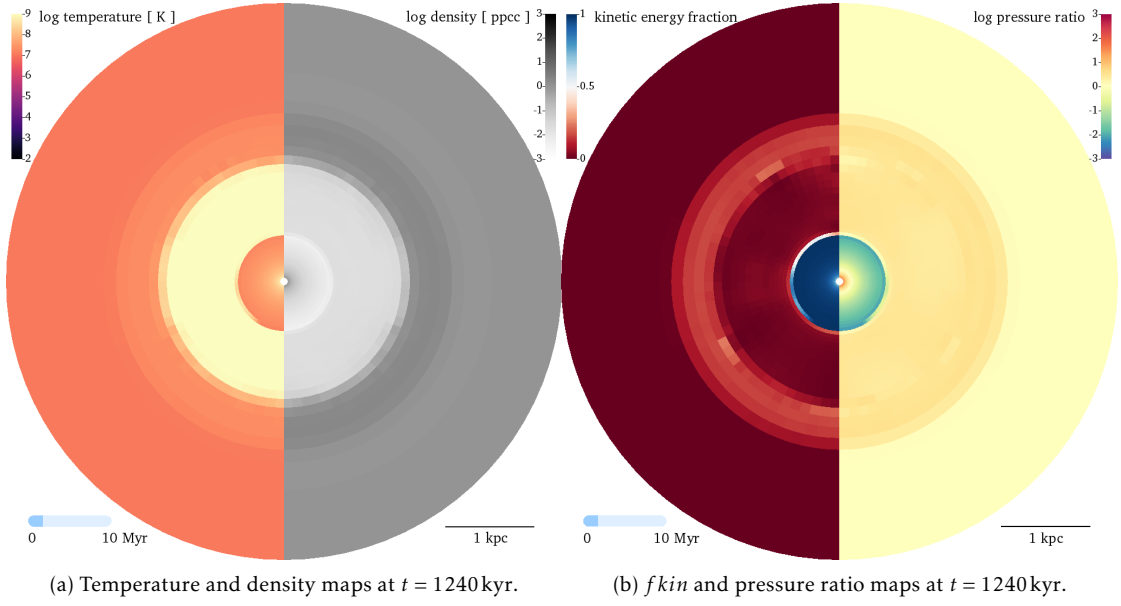


Figure 7: Snapshot of a  $M = 3$  wind without clouds (run Dn) showing the two-shock structure of a spherical wind.

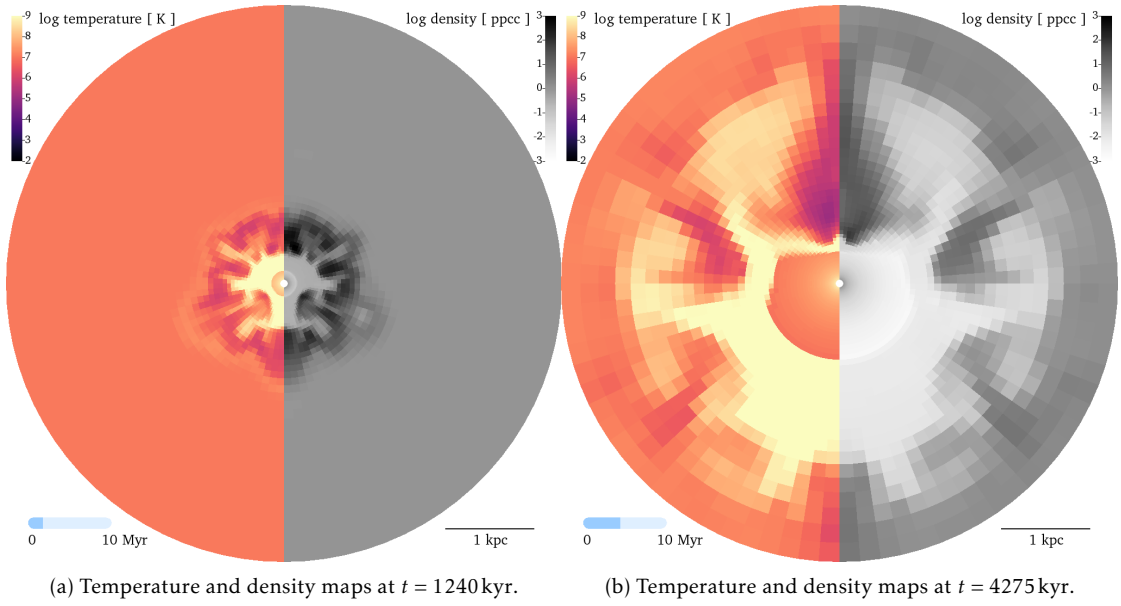


Figure 8: Evolution of the temperature and density of simulation Da, the case for  $M = 3$  that precludes radiative cooling.

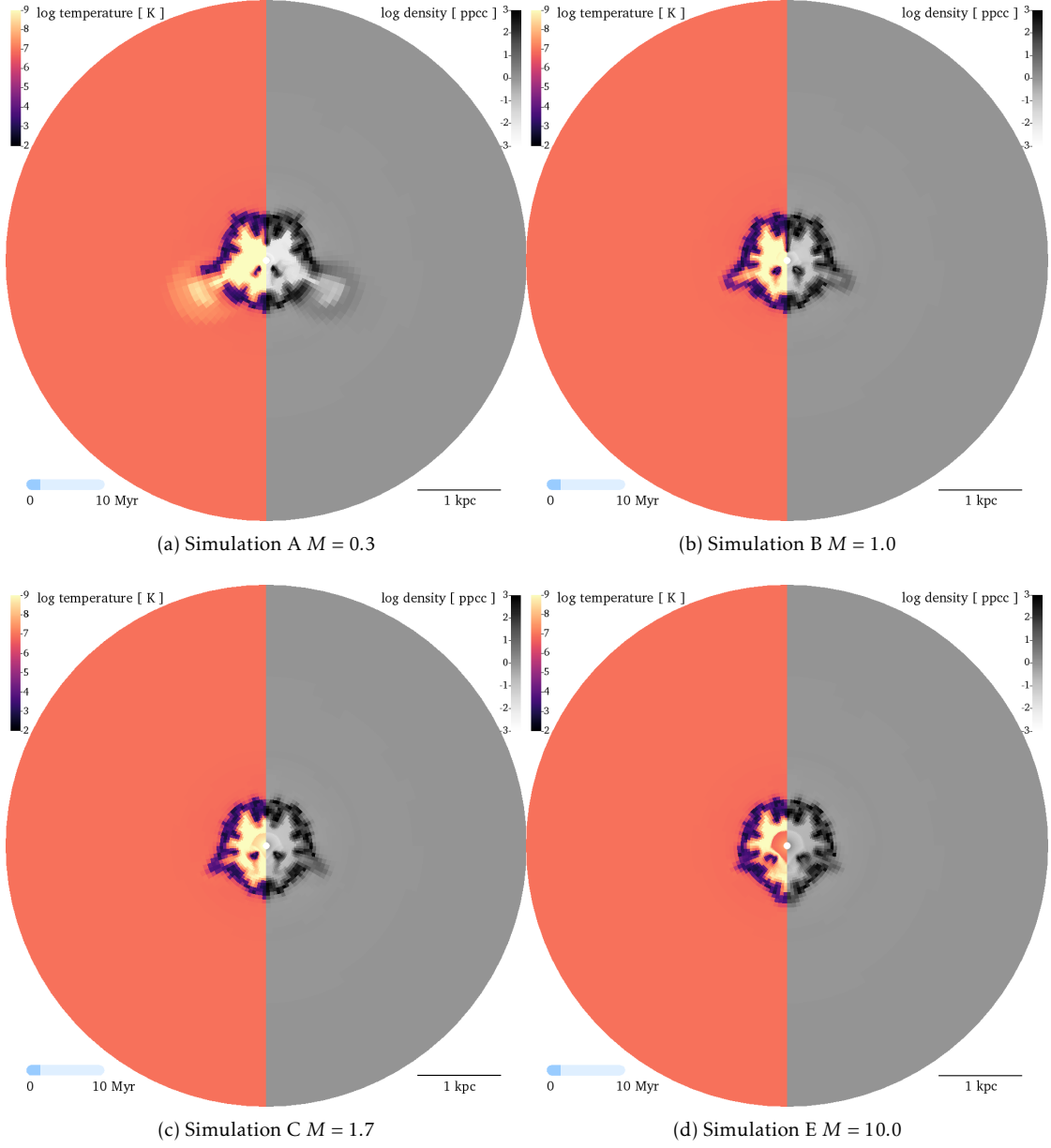


Figure 9: Comparison of simulations at the same time snapshot at  $t = 1.25$  Myr.



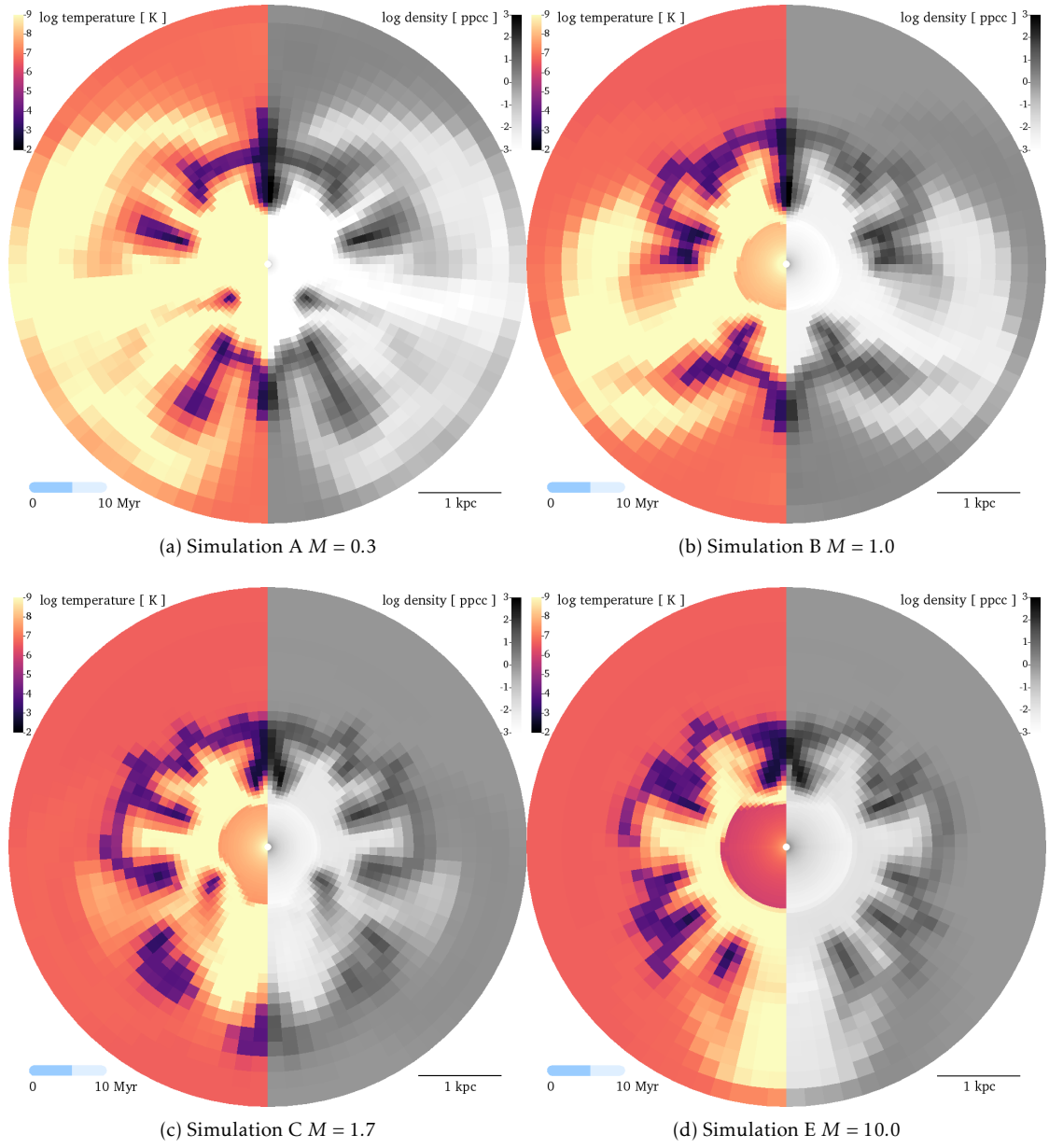


FIG 10: Comparison of simulations at the same time snapshot at  $t = 5.5$  Myr.

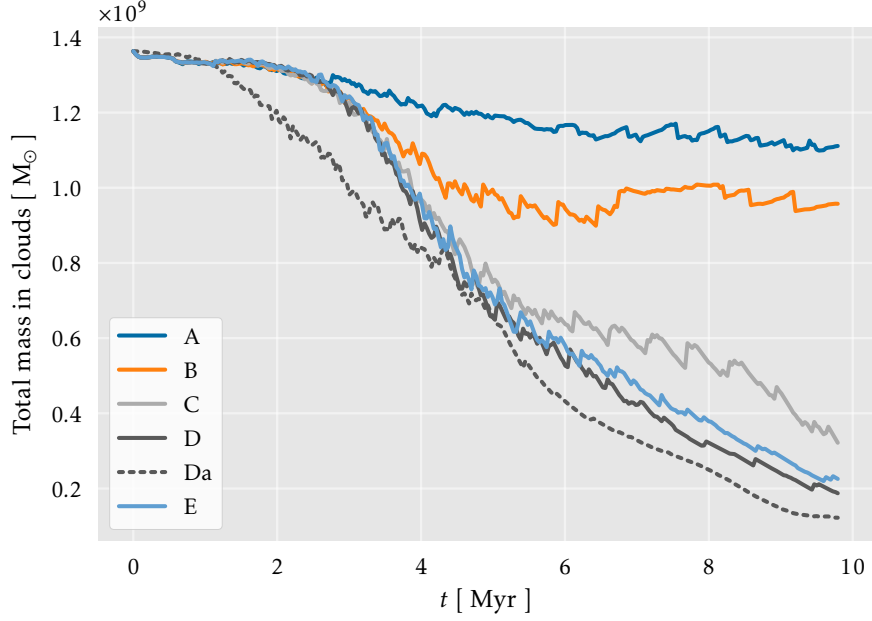


Fig. 11: Evolution of the mass in clouds (cloud tracer cut at 0.98) with time. The curves first proceed the same, then diverge at around  $t = 3$  Myr.

As we mentioned, the mass in clouds declines with time (Fig. 11), implying cloud complexes are being destroyed with time. Clouds suffer from stronger destruction with increasing wind Mach number. The cases for internally subsonic or sonic winds (Mach numbers 0.3, 1.0) exhibit much less cloud destruction rates than simulations with winds of higher internal Mach number (1.7, 3.0, 10.0). The cloud mass-weighted average velocity (Fig. 12) and mass outflow rates (Fig. 13) also show a similar divide. The range of Mach numbers where the change in feedback efficiency is particularly rapid is between  $M = 1.0$  and 1.7. However, the exact physical cause behind the different cloud destruction rates and cloud acceleration are unclear at this point and require more simulations with different parameters.

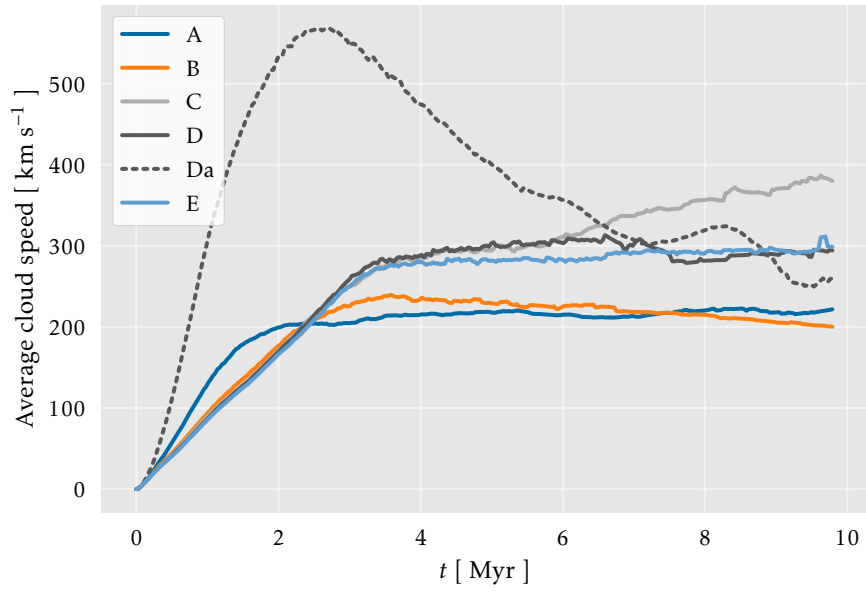


Figure 12: Evolution of the mass-weighted average velocity of clouds (cloud tracer cut at 0.98) with time. The curve is steep first, then flattens, showing two groups that differ in speed by about  $100 \text{ km s}^{-1}$ .

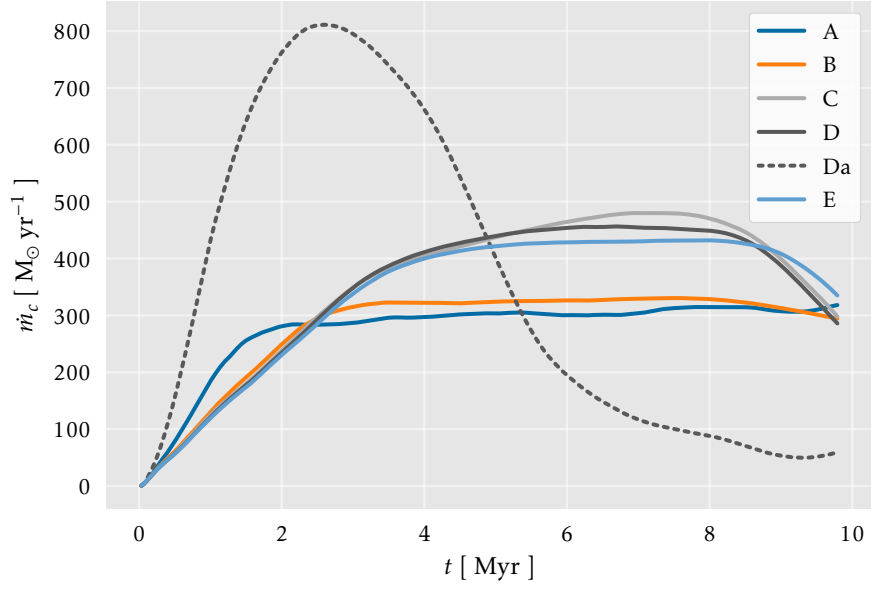


Figure 13: Evolution of the cloud mass outflow rates (cloud tracer cut at 0.98) with time. The curve is steep first, then flattens and divides into two groups differing in mass outflow rates by about  $100 M_{\odot} \text{yr}^{-1}$ . The drop toward the end is caused by the outflow leaving the computational domain.

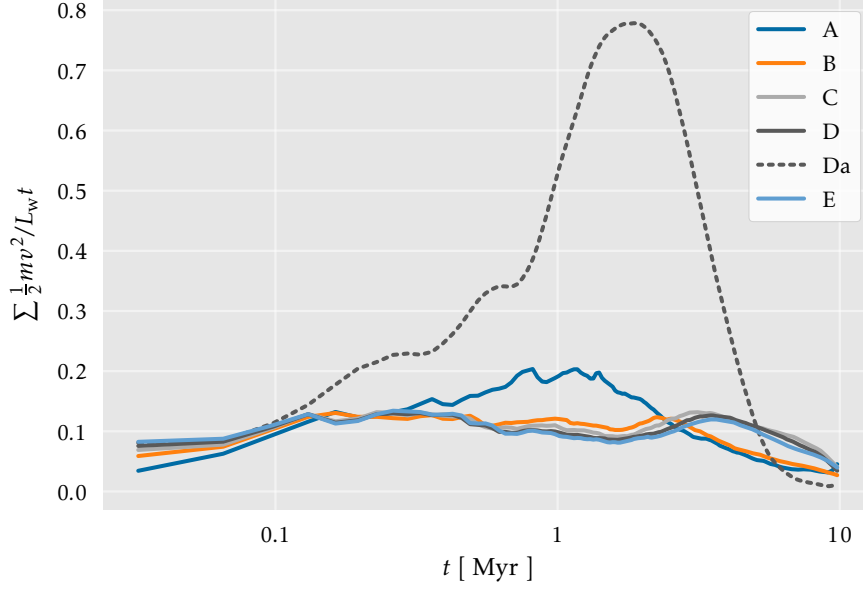


Fig. 14: Evolution of the kinetic energy efficiency in outflowing clouds (cloud tracer cut at 0.98) with time. All curves except Da fluctuate around 0.1 regardless of Mach number.

The fraction of wind energy going into kinetic energy in outflowing clouds (Fig. 14) is almost constant at 0.1, regardless of Mach number.

The momentum boost, shown in Fig. 15, is the evolution of the momentum in clouds normalized by total injected bulk momentum with time. In all simulations, the clouds experience a momentum boost greater than unity. Especially for simulations in which  $f_{\text{kin}}$  is small, that is, for simulations in which the bulk momentum injected through the wind is small, the momentum boost is large because the thermal energy provides additional momentum transfer through thermal pressure gradients.

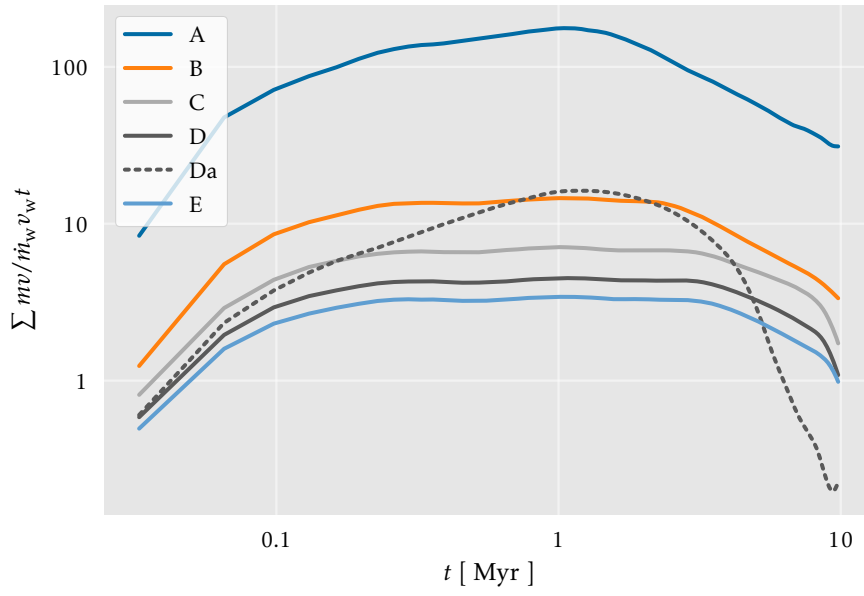


Figure 15: Evolution of the momentum in clouds normalized by injected bulk momentum with time. This quantity is often referred to as the momentum boost.

## 4 Summary and discussion

In this work we have shown how the efficiency of AGN feedback as given by various diagnostics depends on the internal Mach number of the wind through two-dimensional spherically-polar hydrodynamic simulations. The internal Mach number of the wind is a measure of  $f_{\text{kin}}$ , the fraction of wind energy at the point of injection that is in kinetic energy; the lower  $f_{\text{kin}}$ , the higher the enthalpy of the wind. To assess the feedback efficiency, we calculated the time-evolution of the following quantities in each of the simulations:

1. The mass in clouds varies greatly depending on the number of Mach, and cloud destruction (decrease of mass) reduce with the Mach number increasing.
2. The maximum speed of cloud accelerated by wind and mass outflow rate change by Mach number is about 50%.
3. Kinetic energy efficiency is about 0.1, almost independent of Mach changes.
4. The normalized momentum exceeds unity (the momentum boost) and increases with increasing Mach number.

The feedback efficiency in terms of the velocities the clouds reach and the mass outflow rates the clouds reach only varied by at most 50% as the internal Mach number was varied. [Wagner et al. \(2012\)](#) showed that if AGN feedback is important in determining the  $M$ - $\sigma$  relation, the scatter due to differing ISM conditions, e.g. density, porosity, or size-scale clouds, can lead to a scatter in the velocity of clouds of a factor of a few. In comparison to this, the scatter due to varying internal Mach in winds appears secondary.

The fraction of wind energy imparted to kinetic energy of the clouds is about 0.1 for all simulations, regardless of whether the initial wind was dominated by enthalpy or by kinetic energy. For winds in which the enthalpy dominates, this work showed that the large momentum boost ensures sufficient acceleration of the clouds.

The winds with different internal Mach number appear to have different effects on the destruction, dispersal, and mixing of clouds. The winds with higher Mach number, which are kinetic-energy dominated cause a more rapid destruction of clouds than winds that are enthalpy dominated. One possible explanation of this is that the ram-pressure in streams of wind plasma in kinetic-energy dominated winds breaks up clouds as they are accelerated, while the thermal pressure in enthalpy-dominated winds accelerates the clouds more uniformly, leading to less fragmentation.

Serving as test problems, the simulations in this work were designed to complete in a short time allowing immediate analysis. The low grid resolution could certainly be increased. For example, increasing the resolution by a factor of 2 in each dimension would require a factor of 8 longer computational time. More important, however is to perform these simulations in 3D. The two-dimensional geometry in this work represents an unnatural cloud distribution; inhomogeneities such as clouds in 2D axis-symmetric spherical polar coordinates are therefore toroidal if revolved around the axis of symmetry. The clouds near  $\theta = 0^\circ$  and  $\theta = 180^\circ$  represent much smaller cloud masses than that of an identical cloud (with the identical cross-sectional area) at the same radius but at  $\theta = 90^\circ$  would. It is also well known that two-dimensionally confined turbulence, as is the case here, behaves very differently than three dimensional turbulence, since vortices in the flow cannot cascade down into smaller eddies along their axis of rotation. Full 3D simulations are therefore vital to make sure these results hold for realistic cloud distributions in three dimensions.

Regarding the choice of parameters, with the current set of simulations it is not possible to disentangle the physical reasons for why certain simulations produce higher or lower feedback efficiencies for certain measures of efficiency. To gain more insight, series of simulations with parameters that change in different ways on the plane shown in Fig. 2 need to be examined. For example, one could keep the mass injection rate of the wind constant while changing the velocity. Alternatively, one could keep the density or pressure of the wind constant while changing the Mach number. These simulations could shed light into which parameters of the wind are most responsible for higher or lower feedback efficiencies.

The analysis of the various measures for feedback efficiency made use of the cloud tracer variable and an associated cutoff to identify the remains of the initial clouds at later times. The results almost certainly depend on the choice of the cutoff value, although it is not expected that the relative trends presented in this work change. More interesting would be an analysis that identified clouds based on their thermodynamic properties; For example, clouds could be identified as having a temperature and density below some critical values. Such a method would enable the identification of clouds that were formed as a result of rapid cooling behind shocks or in mixing layers. The simulations certainly show a substantial amount of additional dense cool material forming in mixing layers, and it would be interesting quantifying the mass of newly formed clouds, an effect that could be associated with positive feedback, since molecules and stars could form in such dense regions.

Despite the caveats mentioned above, the results of this study are sufficiently encouraging to motivate full 3D high-resolution simulations of this problem.



## 参考文献

- Bieri, R., Dubois, Y., Rosdahl, J., et al. 2017, MNRAS, 464, 1854
- Colella, P., & Woodward, P. R. 1984, J. Comput. Phys., 54, 174
- Fabian, A. C. 1999, Mon. Not. R. Astron. Soc., 308, L39
- Ferrarese, L., & Merritt, D. 2000, Astrophys. J., 539, L9
- Harrison, C. M., Costa, T., Tadhunter, C. N., et al. 2018, Nature Astronomy, 2, 198
- King, A. 2003, ApJ, 596, L27
- Lewis, G. M. G. M., & Austin, P. H. P. H. 2002, in 11th Conference on Atmospheric Radiation, ed. G. H. Smith & J. P. Brodie, American Meteorological Society Conference Series (45 Beacon Street Boston, MA 02108: American Meteorological Society), 123–126
- McConnell, N. J., & Ma, C.-P. 2013, Astrophys. J., 764, doi:10.1088/0004-637X/764/2/184
- Mukherjee, D., Bicknell, G. V., Sutherland, R., & Wagner, A. 2016, MNRAS, 461, 967
- Mukherjee, D., Bicknell, G. V., Wagner, A. e. Y., Sutherland, R. S., & Silk, J. 2018, MNRAS, 479, 5544
- Naab, T., & Ostriker, J. P. 2017, Annu. Rev. Astron. Astrophys., 55, 59
- Rodighiero, G., Brusa, M., Daddi, E., et al. 2015, The Astrophysical Journal Letters, Volume 800, Issue 1, article id. L10, 5 pp. (2015)., 800, L10
- Schindler, J.-T., Fan, X., & Duschl, W. J. 2016, Astrophys. J., 826, doi:10.3847/0004-637X/826/1/67
- Silk, J., & Rees, M. J. 1998, Astronomy and Astrophysics, v.331, p.L1-L4 (1998), 331, L1
- Smits, A. J., Spina, E. F., Alving, A. E., et al. 1989, Physics of Fluids A: Fluid Dynamics, 1, 1865
- Sutherland, R. S., & Bicknell, G. V. 2007, Astrophys. J. Suppl. Ser., 173, 37
- Sutherland, R. S., & Dopita, M. A. 2017, Astrophys. J. Suppl. Ser., 229, 26
- Wagner, A. Y., & Bicknell, G. V. 2011, ApJ, 728, 29
- Wagner, A. Y., Bicknell, G. V., & Umemura, M. 2012, ApJ, 757, 136
- Wagner, A. Y., Bicknell, G. V., Umemura, M., Sutherland, R. S., & Silk, J. 2016, Astronomische Nachrichten, 337, 167
- Wagner, A. Y., Umemura, M., & Bicknell, G. V. 2013, ApJ, 763, L18
- Weinberger, R., Springel, V., Pakmor, R., et al. 2018, Mon. Not. R. Astron. Soc., 479, 4056